

# Inverted Ionization Zones in Eta Carinae’s “Weigelt Knots”<sup>1</sup>

Grant N. Remmen<sup>2,3</sup>, Kris Davidson<sup>2</sup>, Andrea Mehner<sup>4</sup>

Received \_\_\_\_\_; accepted \_\_\_\_\_

---

<sup>1</sup>Based on observations made with the NASA/ESA *Hubble Space Telescope*. STScI is operated by the association of Universities for Research in Astronomy, Inc. under the NASA contract NAS 5-26555.

<sup>2</sup>School of Physics and Astronomy, University of Minnesota, Minneapolis, MN 55455

<sup>3</sup>California Institute of Technology, Pasadena, CA 91125

<sup>4</sup>ESO, Alonso de Cordova 3107, Santiago de Chile

## ABSTRACT

The Weigelt knots, dense slow-moving ejecta near  $\eta$  Car, are mysterious in structure as well as in origin. Using a special set of spectrograms obtained with the *HST*/STIS, we have partially resolved the ionization zones of one knot to an accuracy of about 10 mas. Contrary to simple models, higher ionization levels occur on the *outer* side of the knot, i.e., farther from the star. They cannot represent a bow shock, and no truly satisfying explanation is yet available – though we sketch one tentative possibility. We emphasize that STIS spectrograms provide far more reliable spatial measurements of the Weigelt Knots than *HST* images do, and this technique can also be applied to the knots’ proper motion problem.

*Subject headings:* circumstellar matter - stars: emission-line, Be - stars: individual (eta Carinae) - stars: variables: general - stars: winds, outflows

## 1. The Weigelt Knots

Many years ago, speckle imaging techniques revealed compact brightness peaks within  $0.3''$  of  $\eta$  Carinae (Weigelt & Ebersberger 1986; Hofmann & Weigelt 1988). Observations with the *Hubble Space Telescope (HST)* later showed emission-line spectra there (Davidson et al. 1995, 1997; Weigelt & Kraus 2012; Hamann 2012).

Often called the ‘‘Weigelt knots’’ or ‘‘Weigelt blobs,’’ these objects have extraordinary attributes: (1) They move outward from the star at much lower speeds than  $\eta$  Car’s other ejecta,  $V \sim 40 \text{ km s}^{-1}$  instead of  $V > 300 \text{ km s}^{-1}$ ; (2) they were ejected significantly later than the star’s Great Eruption of 1830–1860 (Weigelt et al. 1995; Davidson et al. 1997; Dorland et al. 2004; Smith et al. 2004); and (3) they produce thousands of narrow emission lines of  $\text{Fe}^+$ ,  $\text{Fe}^{++}$ , and other species (Zethson 2001; Zethson et al. 2012). They are rather dense by nebular standards,  $n_H > 10^7 \text{ cm}^{-3}$ . Doppler shifts and astrometry indicate locations 300–1000 AU from the central star, and fairly close to the equatorial plane of the bipolar Homunculus ejecta-nebula. Most authors suspect an origin in the ‘‘second eruption’’ observed around 1890 (e.g. Weigelt et al. 1995; Davidson et al. 1997; Smith et al. 2004; Smith 2012; Weigelt & Kraus 2012); but, for reasons noted in §2 below, this surmise is difficult to prove. Indeed, since infrared images do not closely match visual-wavelength data (Artigau et al. 2011), the features may conceivably be illusions caused by local minima in the circumstellar extinction, rather than physical condensations. In summary, the Weigelt knots are known only in a rudimentary sense, and they have certainly not been explained.

Their emission lines are presumably excited, directly or indirectly, by radiation from the central binary star. Observed spectra appear consistent with this hypothesis (Hamann 2012), and alternatives such as shock excitation have serious energy-supply difficulties (§5 below). Therefore the knots’ spectra and ionization structure contain valuable information about the UV output of both central stars, if we can understand and quantify the

morphology. In this paper we report the first observations of spatial ionization structure in a Weigelt knot.

The Fe II, [Fe II], and other low-ionization features result from a combination of UV fluorescence plus ordinary thermal collisions in H<sup>0</sup>/H<sup>+</sup>, He<sup>0</sup> zones (Hamann 2012). The He I, [Ne III], and [Ar III] lines, however, arise in He<sup>+</sup> zones which require helium-ionizing photons,  $h\nu > 25$  eV. Since the primary star is too cool, these are thought to be supplied by the hot secondary star, see Mehner et al. (2010) and refs. therein. Based on likely parameters, one expects high-ionization zones of He<sup>+</sup>, Ne<sup>++</sup>, etc., to exist in parts of the Weigelt knots that face toward the central star (Osterbrock & Ferland 2006; Davidson & Netzer 1979). In other words, the simplest model predicts an inverse correlation between ionization level and distance from the star. The size scale of the zones should help to constrain the local density values and the FUV output of the secondary star.

Here we describe spatially resolved measurements of ionization zones in Weigelt knot ‘C’. But our main result is counter-intuitive, almost paradoxical: *the stratification appears to be inverted*, with higher ionization at larger projected distances from the central star. No satisfying explanation has yet been proposed.

## 2. Observational Difficulties, and a Method based on Spectrograms

Three main unsettled observational problems require spatial resolution of the Weigelt knots: their proper motions, sizes, and ionization structure. Standard *HST* imaging (see, e.g., Dorland et al. 2004, Smith et al. 2004, Weigelt & Kraus 2012, and refs. therein) has proven inadequate for several reasons.

1. The image of the central star seriously contaminates those of the knots. With most available filters the peak brightness of each knot is less than 4% that of the central

star, and the instrumental point spread function (psf) has intricate structure at comparable levels out to  $r \sim 0.3''$ .<sup>1</sup> An example of the small knot/star brightness ratio will be noted at the end of §3.3 below.

2. Standard processing techniques do not fully remove the central star from *HST* images. Experience shows that simple linear subtraction leaves illusory features around  $r \sim 0.2''$ , weak but sufficient to perturb any measurement of the Weigelt knots. Worse, the same is true for standard deconvolution procedures. The reasons are beyond the scope of this paper, but concrete examples can be seen in Figs. 1–3 of Smith et al. (2004). Those authors attempted to deconvolve *HST*/ACS (Advanced Camera for Surveys) images of  $\eta$  Car, but their results show obvious remnants of a circular “ring of beads” which is part of the *HST*’s basic psf (Krist et al. 2011 and refs. therein). In later ACS images with different *HST* roll angles, some of those spots rotated with the instrument.<sup>2</sup>
3. Every *HST* image of the Weigelt knots samples a mixture of continuum plus emission lines. Since the continuum largely represents dust-reflected light from the star, its spatial distribution very likely differs from that of the line-emitting gas (Hamann 2012; Artigau et al. 2011). In order to estimate the relative contributions, one must examine spectra as discussed below.

---

<sup>1</sup> The one relevant exception is narrow-band filter F631N used with the Wide Field Camera (*HST*/WFPC2). In an image made with this filter, 10–20% of the Weigelt-knot signal may represent [S III]  $\lambda 6314$  (Mehner et al. 2010). But most of the signal is due to other emission and/or reflection, and images give no information about the relative contributions. Moreover, the *HST* psf is relatively broad at  $\lambda > 6000 \text{ \AA}$ .

<sup>2</sup> J. Ely 2010, priv. comm.; unpublished data analyses.

These circumstances cast serious doubt on any measurements of the knots in *HST* images. A few special near-IR images are better (see, e.g., Fig. 4 in Artigau et al. 2011), but there are not enough of them to give much information about ionization structure, motions, etc.

The difficulties become far less serious if we employ *HST* slit spectrograms rather than images. Many of the Weigelt knots’ emission lines have peak brightnesses far above the continuum. Moreover, we can take advantage of the narrowness of these lines ( $\Delta V < 60$  km s<sup>-1</sup>) to measure and remove contamination by the underlying star image. The Space Telescope Imaging Spectrograph (STIS) is well adapted to this task.

Apart from complications noted in §3, our basic approach is fairly obvious. Figure 1 shows a small wavelength interval in a fictitious, idealized slit spectrogram. Light source A is the central star and C is one of the Weigelt knots. For simplicity, the star’s spectrum is depicted as a continuum. Two emission lines of C can be seen in the figure, and here we measure the one on the right. If  $x$  denotes spatial position along the slit, we extract two separate spatial samples  $f(x)$ : sample 1 avoids spectral features in both A and C, while sample 2 includes the chosen emission line in C. Each of these can be a STIS/CCD column or a sum of adjoining columns. After sample 1 is renormalized to correct for the wavelength dependence of the continuum flux, the difference  $f_2(x) - f_1(x)$  represents only the emission line arising in knot C. If the spatial profile  $f_1(x)$  depends on wavelength, we can parametrize it by extracting more samples.

In practice this approach works quite well (§3.3). The star subtraction is simpler and more robust than one can achieve in an *HST* image, because it requires only data from a small vicinity on the same spectrogram. (In order to remove the star’s optical halo from an ordinary image, either by subtraction or by deconvolution, one must derive the structure of its image based on optical modeling or another star image; and  $\eta$  Car’s profile probably differs from a point-source psf. The spectrogram method practically eliminates

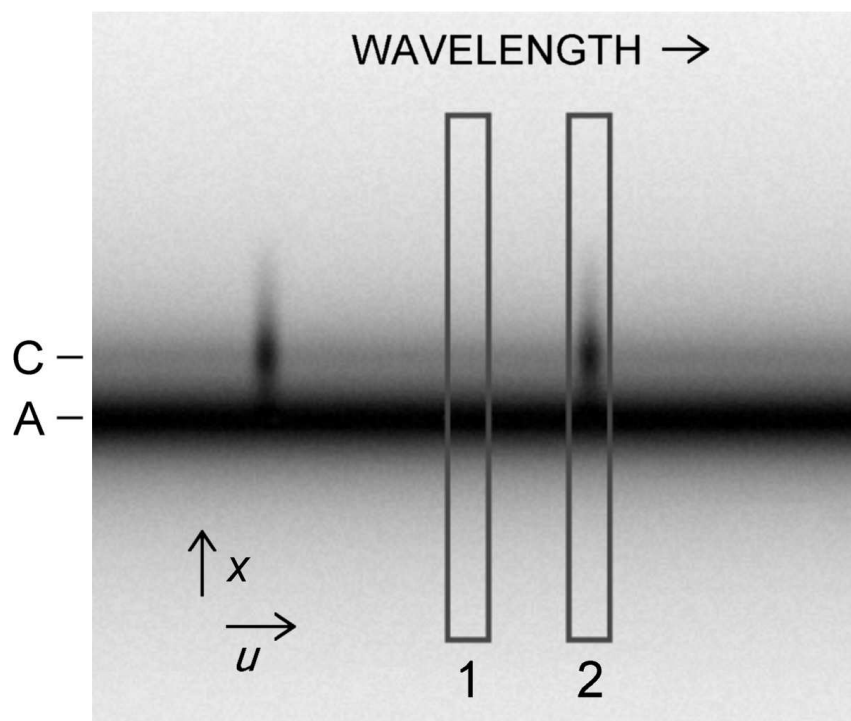


Fig. 1.— Narrow wavelength interval in a simulated spectrogram, showing our basic measurement procedure. ‘A’ and ‘C’ are the spectra of the central star and of Weigelt knot C; two narrow emission lines of the latter can be seen. Various complications are noted in the text.

this difficulty.) A mild non-linearity of the detector response would invalidate conventional methods of removing the central star optical halo in an image, but has only a second-order influence with our method. And, most important, for many narrow emission lines the brightness ratio  $C/A$  is far greater than in any available non-spectroscopic image.

In order to obtain adequate spatial sampling with the STIS/CCD, one must employ “dithered” observations (§3). Since no such data were obtained before 2010, we have not yet attempted to apply our method to the proper motion and ejection-date puzzle. Instead we focus on another, equally significant problem: the knots’ ionization structure mentioned in §1 above.

We chose narrow emission lines in four physically distinct categories:

- (A) Low ionization: Fe II, [Fe II], and other species that can occur in either an  $H^0$  or an  $H^+$  zone.
- (B) Moderate ionization: [Fe III]. Since the ionization potential of  $Fe^+$  is 16.2 eV,  $Fe^{++}$  tends to coexist with  $H^+$  and  $He^0$ .
- (C) High ionization: He I, [Ar III], and [Ne III], representing  $He^+$  zones. (The He I lines are due to recombination.)  $He^0$ ,  $Ar^+$ , and  $Ne^+$  have ionization potentials of 24.6, 27.6, and 41.0 eV, presumably requiring photons from the hot secondary star. See Mehner et al. (2010) and refs. therein.
- (D) Exotic: Fe II  $\lambda\lambda 2508, 2509$ . Pumped by  $Ly\alpha$ , these extraordinary features have laser-like properties almost unique in astrophysics (Johansson & Letokhov 2004; Hamann 2012; Johansson & Hamann 1993; Davidson et al. 1997).

The high ionization lines were once suspected to come either from a diffuse region in which the Weigelt knots are imbedded, or perhaps from gas between the star and the knots (Verner et al. 2005). Mehner et al. (2010) showed, however, that [Ne III] has brightness maxima near the knots. Data available for that investigation could not resolve each knot.



If the knots are real density concentrations, then the nature of photoionization leads one to predict stratified ionization zones as noted in §1 above. The relative location of Fe II  $\lambda\lambda 2508, 2509$  is potentially valuable because it is model-dependent: it might occur in the moderate ionization zone because Ly $\alpha$  photons from the stellar wind have difficulty penetrating the low ionization zone, and some Fe<sup>+</sup> ions coexist with Fe<sup>++</sup>.

We measured the nineteen emission lines listed in Table 1. Suitable data were available in four wavelength intervals (§3), and we chose well-defined isolated lines, avoiding substantial features in the star’s spectrum. For instance, we omitted [Ne III]  $\lambda 3969$  because it is confused with other strong features. [Ar III]  $\lambda 7138$  has too long a wavelength for *HST*’s best resolution, but it gave useful results (§4). Spectral traces in Figure 2 show most of the selected emission lines. The UV spectral region is omitted because  $\lambda\lambda 2508, 2509$  hugely exceeds all other features there; see, e.g., Fig. 8 in Davidson et al. (1997), Fig. 5.5 in Hamann (2012), and Fig. A.3 in Zethson et al. (2012).

### 3. The Data Set and Detailed Methods

Since our procedure was carefully adapted to a non-routine purpose, it requires a lengthy explanation. Readers interested mainly in the results, and willing to trust our precautions, may choose to skip most of this section.

The STIS/CCD has a serious deficiency: its 50.7 mas pixel size is too large to take good advantage of *HST*’s spatial resolution in any single exposure (Davidson 2006). Fortunately the spatial sampling can be improved by “dithering,” i.e., by taking separate observations at positions that differ by (integer + 0.5) pixels along the spectrograph slit. Data of this type were obtained on 2010 March 3, as listed in Table 2. The slit was oriented along position angle 302° (close to NW by W), sampling the star and knot C (Weigelt & Kraus

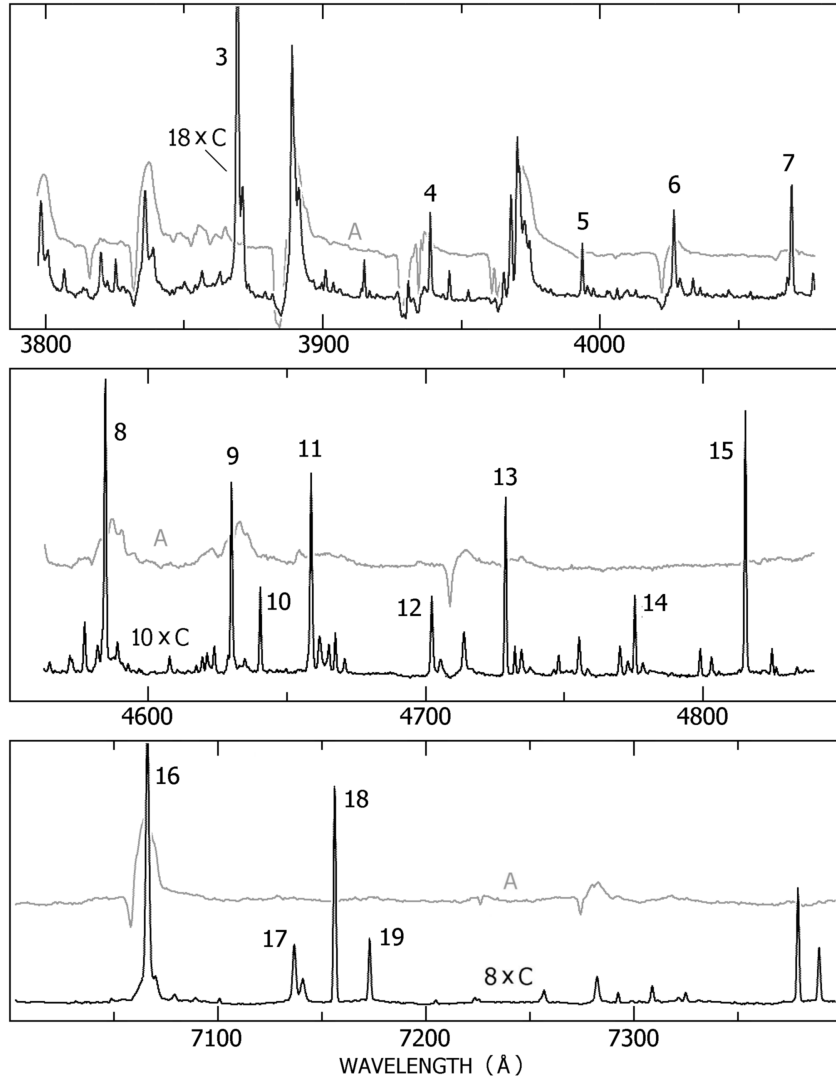


Fig. 2.— HST/STIS spectra showing the emission lines listed in Table 1. Gray tracings represent the central star, while black tracings represent Knot C with magnified flux scales.

2012). Two nominal slit positions were used, with the same midline and differing in the observing plan by  $\Delta x \approx 228 \text{ mas} \approx 4.5$  pixels along the slit. The 4.5-pixel difference, rather than 0.5, ensures that each  $x$ -locale is sampled by two different sets of physical pixels. We measured the true offsets  $\Delta x$  as explained below. The available observing time allowed only enough wavelength coverage to include the best moderate and high excitation features plus [Fe II]  $\lambda\lambda 2508, 2509$  (Mehner et al. 2010; Hamann 2012).

Instead of the “drizzling” process usually applied to dithered *HST* images, we used a careful procedure described below. Since it requires the original, geometrically unaltered CCD rows and columns, we worked with “semi-raw” data: flat-fielded, with cosmic ray hits and average underlying count levels removed, but omitting wavelength calibration and corrections for optical distortion. Cosmic ray removal was based on multiple exposures at each dither location (“CR-SPLIT,”  $N$  in Table 2). We considered treating each individual exposure separately and allowing for cosmic ray hits at a later stage in the process, but concluded that this would give little advantage in practice. In fact the final results were consistent enough to be self-verifying.

A few definitions are needed. Let  $u$  and  $x$  denote CCD column and row number respectively, not necessarily integers because they may refer to an interpolated position. To a first approximation,  $u$  represents wavelength while  $x$  represents spatial position along the slit (Fig. 1). If  $F(u, x)$  denotes intensity incident on the detector, then of course the CCD records only  $f(u_m, x_n)$ , the average of  $F$  in each physical CCD pixel. Regarding  $f(u, x)$  as a continuous function, we estimated values between data points by cubic spline interpolation. For the measurements in §§3.2–3.4 below, we used a complete dither pair for each interpolation, so the  $x$ -interval between data points was approximately 0.5 pixel rather than 1 pixel.<sup>3</sup>

---

<sup>3</sup> Along any column in a single STIS spectrogram, spline interpolation gives erratic re-

Deriving  $F(u, x)$  from  $f(u, x)$  is a non-trivial task, but fortunately the main results are apparent from the unenhanced  $f$ -profiles. Our procedure did *not* include deconvolution, mainly because no trustworthy psf was available and also because such a process may amplify the effects of pixel noise and other high-spatial-frequency defects. At any rate it proved to be unnecessary (§§3.4 and 4.4 below).

### 3.1. Measuring the spectral trace

Spatial position is not exactly constant along a given CCD row; a spectrum “trace” – the locus of a point-source continuum across a spectrogram – is slightly tilted and curved. Typically a STIS trace may shift by 1 row in about 150 columns ( $dx/du \sim 0.007$ ), but this slope varies considerably among the various gratings and grating tilts. Routine spectrum extractions take these facts into account, of course; but our problem requires unusual spatial accuracy. We measured the central star’s trace  $x_A(u)$  in each spectrogram to high precision by the following method.

Consider an observed column vector  $f(x)$  at a given  $u$  in one exposure, interpolated so that it is a continuous function. It may be the average of several adjacent columns, avoiding emission features. Local interpolation errors due to inadequate spatial sampling have very little effect when this procedure is completed. The centroid of  $f(x)$  is close to the star’s position, but is mildly perturbed by the Weigelt knots, by noise, and especially by asymmetry of the psf. A precise and consistent position measure can be obtained as follows.

---

sults because of the inadequate sampling (Davidson 2006). Interpolation within a properly dithered data set is far more satisfactory. Strictly speaking, our interpolation procedure included additional sub-steps that turned out to be unnecessary. We omit them here because they had no practical effect and explanations would be very lengthy.

First adopt a local weighting function  $\phi(s) = 1 - (s/a)^2$  for  $|s| < a$  and 0 elsewhere, with  $a = 4$  pixels  $\approx 203$  mas. At any given position  $x$  along the column, define a local quantity:

$$X(x) = \frac{\int x' f(x') \phi(x' - x) dx'}{\int f(x') \phi(x' - x) dx'}. \quad (1)$$

Thus  $X > x$  or  $X < x$ , respectively, on each side of the major peak of  $f(x)$  due to the star.

A robust modified-centroid location  $x_A$  is then defined by

$$X(x_A) = x_A. \quad (2)$$

Function  $\phi(s)$  suppresses pixels that add noise but little information, and it also reduces pixelization effects.

For any given CCD column  $u$ , we search for the position  $x_A$  that exactly satisfies (2), and we adopt it as the position of the star in that column. If an asymmetric psf causes  $x_A$  to differ from the true position by a small amount, then other spatial features will have the same offset so their *relative* positions  $x - x_A$  are meaningful to high accuracy. We determine the trace  $x_A(u)$  by fitting a cubic polynomial to the values measured in a set of well-spaced columns. A detailed analysis of this method would be too long for this paper, but the main advantages are: (1) it is conceptually simple, (2) the iterative procedure is easy to implement, (3) it averages over pixel noise about as well as any method can, (4) results are consistent without any need to know the parameters of the asymmetric STIS psf, and (5) if enough sample columns are used, the resulting  $x_A(u)$  is quite insensitive to the STIS sampling problems described in Davidson (2006). This last fact is true because the slope of the trace  $dx_A/du$  amounts to “virtual dithering” so far as the cubic fit is concerned. In other words,  $x_A$  coincides with a CCD row in some columns, it falls halfway between row midlines in some other columns, etc., and altogether these average out in the cubic fit.

In each spectrogram listed in Table 2, we chose ten well-spaced column locations  $u$ , corresponding to wavelengths that avoided perceptible emission and absorption lines. For

each of these samples, the adopted  $f(x)$  was the average of 5 adjoining CCD columns centered at  $u$ . Then we used the ten sample values  $x_A(u)$  to compute the least-squares cubic fit for  $x_A(u)$  in that spectrogram. Based only on counting statistics, the formal error of each fit was less than 0.01 pixel or 0.5 mas across most of the observed range of  $u$ . (This statement is based on Monte Carlo simulations.) Systematic effects, e.g. due to the asymmetry of the STIS psf, can be larger but have almost no effect on the relative differences  $x - x_A$  which ultimately determine our results.

Corresponding dither pairs (Table 2) provide an obvious consistency test. Ideally their traces  $x_A(u)$  should differ by a constant  $\Delta x = 4.5$  pixels, the offset specified in the observing plan. In fact, the r.m.s. value of  $(\Delta x - 4.5)$  for the six dither pairs in Table 2 is 0.009 pixel  $\approx$  0.5 mas. Variations across the CCD are larger because of image distortions in the STIS. An example: Evaluating the cubic-fit dither offsets  $\Delta x$  at wavelengths of relevant emission lines in the short-exposure 4565–4845 Å dither pair, we find  $4.484 \lesssim \Delta x \lesssim 4.510$ ; a range of 0.026 pixel  $\approx$  1.3 mas. Altogether, the estimated star position  $x_A(u)$  appears to be consistent within  $\pm 1$  mas at most wavelengths, only 2% of the instrumental resolution. Of course this high quality required a large number of data pixels for each fit. The instrumental variations of spatial scale are negligible for our purposes, partly because we employ only a few of the CCD rows running through the central part of the detector. The main point is that errors in the trace  $x_A(u)$  are much smaller than the effects of interest which exceed 10 mas (§4 below). Some extra tests not worth detailing here were also applied, such as comparisons between independent dither pairs. They all had satisfactory outcomes.

Therefore, when examining the spatial position of an emission line in the Weigelt knot C, we can safely refer to a true spatial coordinate

$$z = x - x_A(u) \tag{3}$$

where  $x_A(u)$  is known to high accuracy.

### 3.2. Subpixel modeling

As noted earlier, dithering along the slit is essential because the STIS/CCD spatial sampling is too sparse to take full advantage of *HST*'s basic resolution.<sup>4</sup> For any given CCD column  $u$ , a dither pair of spectrograms provides two sample vectors:

$$f_n^{(1)} = f(n) \quad \text{and} \quad f_n^{(2)} = f(n + \Delta x - 4), \quad (4)$$

where the dither offset  $\Delta x$  is practically a known constant. (Strictly speaking, it's a known function of  $u$  based on the individual exposures' measured traces  $x_A(u)$ .) The two vectors together provide a sampling interval of about 0.5 CCD-pixel or 25 mas, nearly adequate for *HST*'s resolution according to the Nyquist criterion. For each relevant column or sum of adjoining columns, we used cubic spline interpolation to derive a continuous function  $f(x)$ . (Of course this interpolation employed the true  $\Delta x$  values, not the uniform nominal spacing of 0.50 pixel.) Then we shifted each  $f(x)$  to produce  $f(z)$ , a spatial distribution relative to the star's position (eqn. 3).

We half-expected the two parts of each dither pair to differ perceptibly in their intensities and psf's – due, e.g., to variations of the “jitter” in the *HST* pointing, slight drifts perpendicular to the slit, electronic subtleties, etc. In fact no such differences were found.

### 3.3. Removal of the central object

As noted in §2 and Figure 1, we must subtract a “continuum” spatial profile  $f_1(z)$  from the spatial distribution  $f_2(z)$  measured at each narrow emission line. The underlying

---

<sup>4</sup> This statement is not equivalent to the distinction between  $f(x)$  and  $F(x)$  mentioned earlier, though it is related. See Davidson (2006).

$f_1$  represents mainly the central star but it also includes continuum and dust-reflected light from knot C. In order to estimate the relevant  $f_1$ 's, we sampled spatial profiles at various wavelengths that had no perceptible emission features. In order to avoid biased sampling in the  $x$ -direction, we included pairs of wavelengths whose trace positions  $x_A(u)$  differed by substantially non-integer numbers of pixels (§3.1 above).

Within each observed wavelength interval,  $f_1(z)$  varied with wavelength less than one might expect. The optical diffraction limit by itself would imply a narrower spatial psf near the short-wavelength end of an interval. But this is counteracted by poor STIS focussing on the shorter-wavelength side of the CCD, see Davidson (2006) and the instrument handbook.<sup>5</sup> For instance, we found widths between 1.524 and 1.561 pixels (FWHM) for  $f_1(z)$  across the interval 4585–4810 Å – a range of only 2.4% even though the wavelength varied by 5%.

In each panel of Figure 3, the lower trace  $f_1(z)$  depicts the envelope of 4 separate profiles in that wavelength range. Larger variations were found in the other three wavelength ranges, but for each emission line we used nearby samples of  $f_1(z)$ . In the important case of [Ne III]  $\lambda$ 3870, for example, we found a FWHM between 1.663 and 1.669 pixels across the interval 3850–3950 Å. These  $f_1$  widths represent combinations of the basic instrumental psf, imperfect optical focus, *HST* jitter, and very likely a real non-point-like width of  $\eta$  Car's wind; for our purposes there is fortunately no need to know the relative size of each effect. The star's spectrum is more complex at UV wavelengths 2480–2680 Å, but the strange Fe II  $\lambda\lambda$ 2708,2709 lines are extremely bright in the Weigelt knots, easy to separate from the star.

Subtracting  $f_1(z)$  from each narrow-emission-line profile  $f_2(z)$  therefore presented no serious difficulty. This is manifestly true for the brightest measured lines, which considerably

---

<sup>5</sup> <http://www.stsci.edu/hst/stis/handbooks/>.



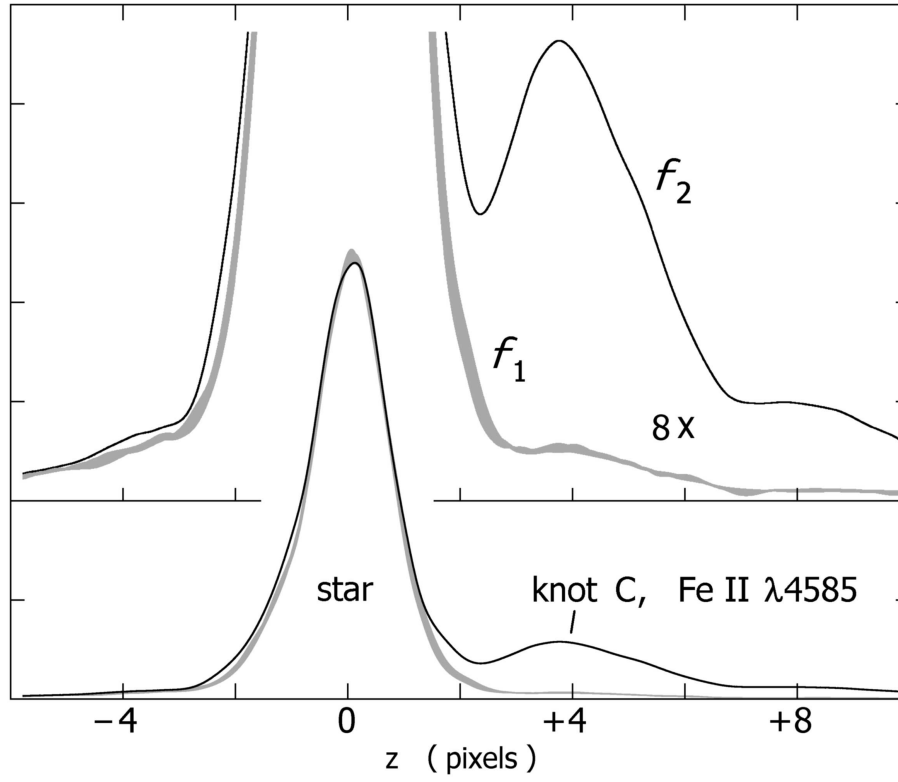


Fig. 3.— Observed spatial profiles along the slit near  $\lambda \sim 4585 \text{ \AA}$ . The two panels differ only in their vertical scales. In each panel, the upper trace  $f_2$  represents a wavelength at the center of the Fe II  $\lambda 4585$  emission line. The lower trace  $f_1$  shows the *envelope* of four independent samples at wavelengths with no perceptible emission features. The five samples were renormalized so they approximately match in the brightest part of the star image.

exceeded the underlying  $f_1(z)$ . Figure 3 shows one such case, Fe II  $\lambda 4585$  (see Table 1). For each narrow emission line we simply used the measured profile  $f_1$  that was closest in wavelength. In each case  $f_1$  was renormalized to match the integrated brightness of  $f_2$  at the star’s peak. (Strictly speaking, we based the adjustment factor on the maximum values of  $q(z) = \int \psi(z - z')f(z')dz'$  for  $f_1$  and  $f_2$ , where  $\psi$  is a parabolic weighting function only 1 pixel wide. Other definitions give practically the same results.) This renormalization is not exactly valid if the narrow emission line extends across the star image; but any resulting error in the difference  $f_2 - f_1$  is very small at the location of knot C, because  $f_1(z_C) \ll f_1(0)$ , see Fig. 3. In recent years the narrow emission lines along our line of sight to the star have been quite faint compared to the star itself (Mehner et al. 2010).

Figures 4 and 5 show examples of net profiles  $g(z) = f_2(z) - f_1(z)$ . Numerical oscillations occur at the location of the star,  $-2.3 \lesssim z \lesssim +2.3$ , because the net values there are differences between two very large quantities which are nearly equal but slightly imperfect. As one expects from Figure 3, the Weigelt knot is represented quite well for  $z \gtrsim 2.5$  pixels – much better than in any non-spectroscopic *HST* image. Separate dither pairs (independent sets of STIS exposures) gave  $g(z)$  profiles that mutually agreed to within the uncertainties set by counting-noise. He I profiles tend to be less satisfying than the others, for a reason noted in §4 below.

Incidentally, Figure 3 illustrates the difficulty of measuring a Weigelt knot in standard images. In continuum light, knot C appears only as a small bump in the  $f_1$  tracing near  $z \sim 4$  pixels, scarcely brighter than the star’s psf at that location. By contrast, the narrow emission line greatly exceeds the star in that locale; compare curve  $f_2$  to  $f_1$  in the figure.

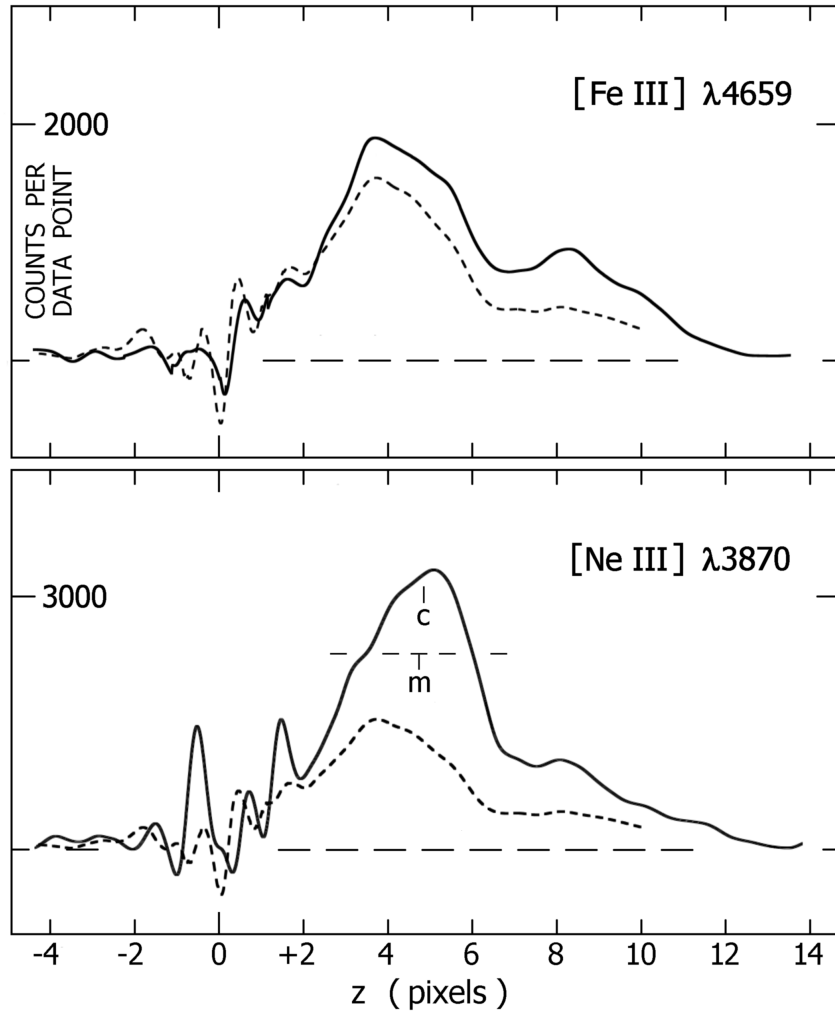


Fig. 4.— Net spatial profiles  $g(z)$  for the [Fe III]  $\lambda 4659$  and [Ne III]  $\lambda 3870$  emission lines in knot C. For the latter, points ‘m’ and ‘c’ are “midpoint” and “centroid” positions defined in §3.4. Dashed curves show the average spatial profile of four [Fe II] lines, see text §4.

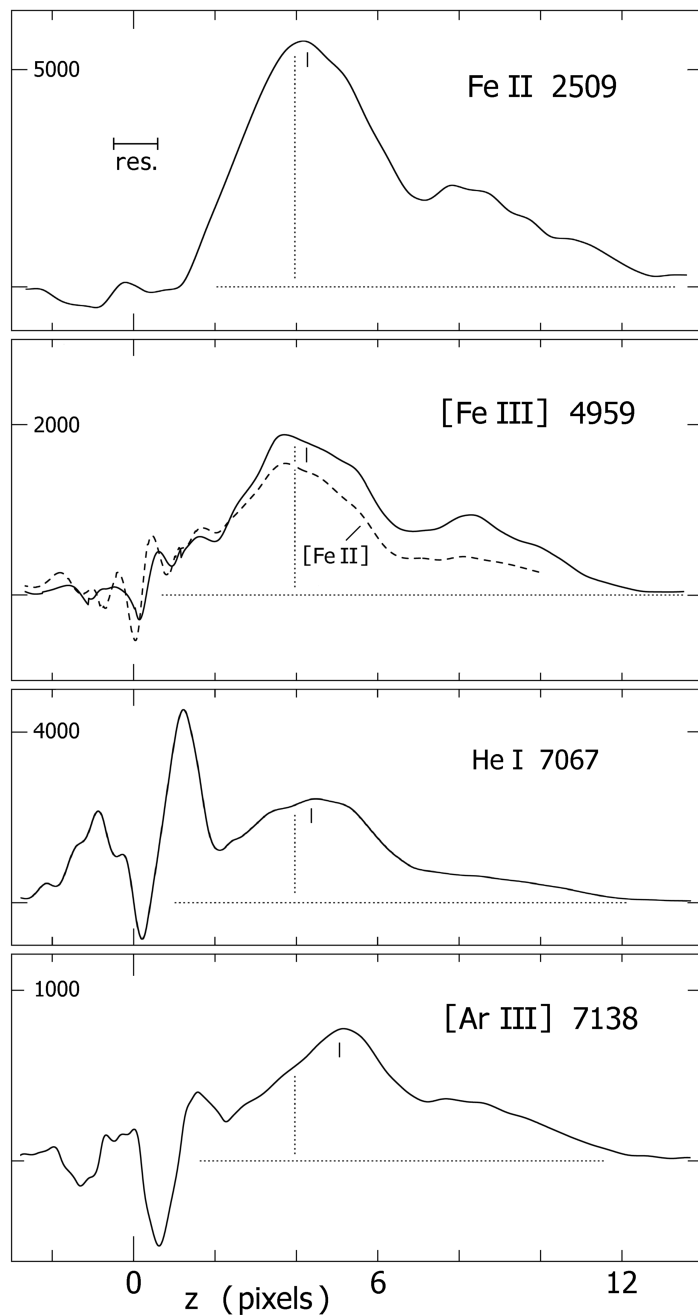


Fig. 5.— Spatial profiles  $g(z)$  for several emission features with differing characteristics. A small vertical mark shows  $\hat{z}$  for each feature, defined in §3.4. The dashed curve is an average of four [Fe II] lines, the same as in Fig. 4. The vertical dashed line shows their average  $\hat{z}$ .

### 3.4. Measuring the positions

The most reliable part of the net spatial profile  $g(z) = f_2(z) - f_1(z)$  is obviously near its peak, see Figures 3 and 4. Therefore we based our position measurements on the 70%-of-peak level. For each narrow emission line the procedure was as follows. Begin with the available dithered data points along the appropriate CCD column, i.e., at half-pixel intervals of  $z$ . Via cubic splines, these define a continuous spatial profile  $g(z)$ . Denote by  $z_a$  and  $z_b$  the two places where  $g(z) = 0.7 g(\text{peak})$ . Then, if  $h(z)$  is the quantity  $g(z) - 0.7 g(\text{peak})$ , one can easily calculate a “midpoint” and “centroid”:

$$z_m = \frac{z_a + z_b}{2} \quad \text{and} \quad z_c = \frac{\int z h(z) dz}{\int h(z) dz}, \quad (5)$$

with integration limits  $z_a$  and  $z_b$ . The difference  $z_c - z_m$  indicates asymmetry near the line peak. Examples are shown in the lower panel of Figure 4. In most cases we use the simple average  $\hat{z} = 0.5 (z_m + z_c)$ .

We estimated statistical uncertainties by performing random simulations with profiles like those shown in Figure 4. Several types of statistical error occur. (1) Most important is the counting noise associated with the square root of  $f_1 + f_2$ . For a net profile  $g$  with a peak of 1500 counts per data point, the resulting rms error in either  $z_m$  or  $z_c$  was found to be roughly  $\pm 0.07$  pixel. Noise errors are of course worse for fainter profiles. (2) Imperfect spatial sampling also has an effect, because the precise cubic-spline fit  $g(z)$  depends on the location of the pixel array relative to the spatial profile. This depends on the profile shape, but we estimated typical rms errors in the range  $\pm 0.003$  to  $\pm 0.01$  pixel. These do not depend on the strength of the emission line. (3) According to §3.1 above, errors in the spectral trace  $x_A(u)$  are not worse than  $\pm 0.03$  pixel. Uncertainties quoted above are formal statistical estimates, and *systematic* errors may be larger (§4.1 below).

In principle, one-dimensional Lucy-Richardson deconvolution can enhance the spatial

resolution; but a few trial examples showed no worthwhile improvement with these data. Knot C appears to be partially resolved without deconvolution, having FWHM  $\sim 3.6$  pixels  $\sim 180$  mas (Fig. 4) – i.e., almost 3 times as wide as the overall psf. Since deconvolution tends to magnify small numerical irregularities and noise at high spatial frequencies, we chose not to employ it here.

#### 4. Results

Figures 4 and 5 show some of the measured spatial profiles  $g(z)$ . As a reference for comparison, in each figure a dashed curve shows the unweighted average of four [Fe II] features labeled 10, 13, 14, 15 in Tables 1 and 3.

The most surprising result concerns spatial location  $z$  as a function of ionization level, shown in Tables 3 and 4 and Figure 6. *Highly excited features obviously tend to occur farther from the star, i.e. at larger  $z$ , not closer to the star as was expected* (§1). Two very different statistical analyses in §4.1 and §4.2 below confirm the reality of this effect.

Before reviewing likely errors, it is important to recall that our measurement procedure was blind to ionization and excitation level; the various emission lines occurred at essentially random columns on the detector, and they were all treated alike. Note also that [Ne III] and [Ar III], the conspicuously highest points in Figure 6, probably represent Category C better than the He I lines do. [Ne III] and [Ar III] originate mainly in the highest-temperature gas, while the He I recombination lines are less sensitive to temperature and tend to favor the coolest parts of the He<sup>+</sup> zones (Osterbrock & Ferland 2006; Davidson & Netzer 1979). Moreover,  $\eta$  Car’s stellar wind produces substantial He I features, which may perturb our He I positional measurements toward slightly smaller values of  $\hat{z}$ ; indeed this is obvious for He I  $\lambda 7067$  in Figure 5. Therefore Table 4 summarizes the  $\hat{z}$  values for two versions of

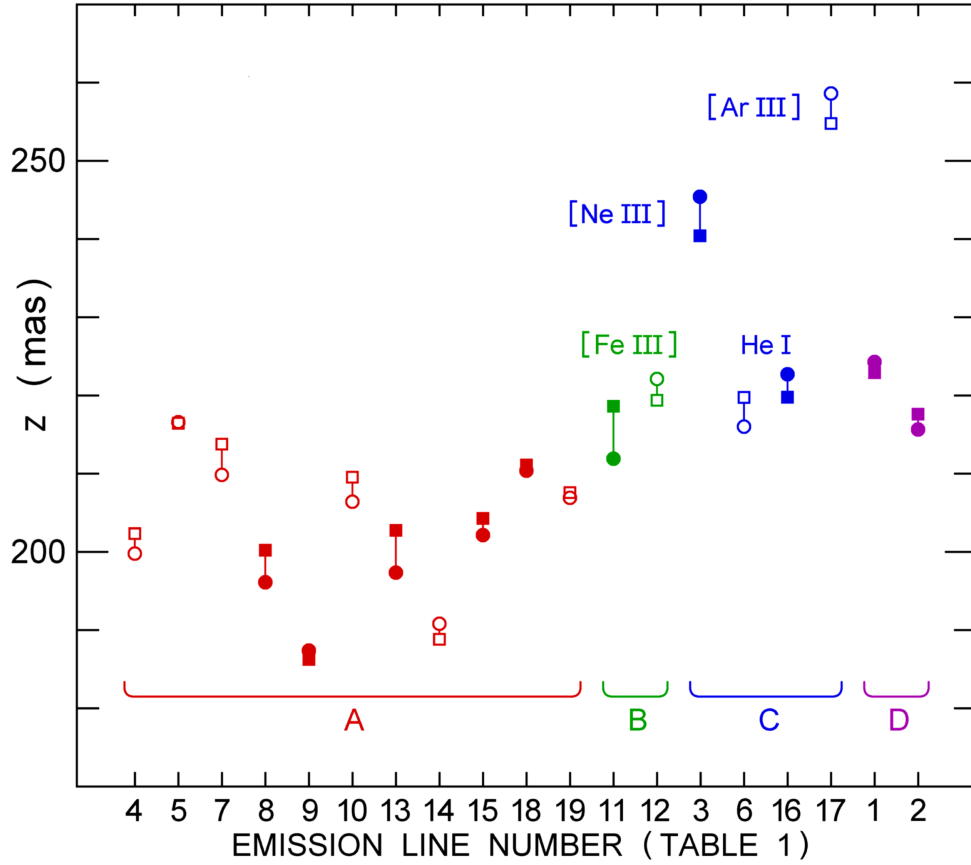


Fig. 6.— Measured distances of emission peaks from the star, sorted by ionization category. These are the results listed in Table 3; filled symbols represent features with higher count rates. Circles and squares indicate  $z_c$  and  $z_m$  respectively, see text.

Category C: with and without the He I lines.

#### 4.1. Statistical significance based on measurement quality

One form of confidence level involves the measurement uncertainty. We can estimate this quantity based on the scatter of either  $z_m$  or  $z_c$  among the nine Fe II and [Fe II] features listed in Table 1. In principle the forbidden lines might differ from permitted lines because the latter have higher upper energy levels; but in fact we find no statistically significant difference between the six [Fe II] lines and the three Fe II features. If all of them have the same true average position, then the scatter in measured values indicates an r.m.s. error of about  $\pm 0.17$  pixel or  $\pm 8.6$  mas for both  $z_m$  and  $z_c$ . This is roughly twice as large as the semi-formal statistical uncertainty estimated in §3.4. Therefore, undiagnosed effects of the order of  $\pm 7$  mas – instrumental subtleties and/or imperfect assumptions about the emission – probably dominate the error budget. This is a common, or even usual, circumstance for sensitive astronomical measurements.<sup>6</sup> Such effects can probably be treated like random errors here, because, as noted above, the wavelengths, detector locations, and intensities were not seriously correlated with emission-line category or excitation. If all the  $\hat{z}$  values are systematically too high or too low, this has no effect on differences between emission categories.

Now consider the unweighted average of  $\hat{z}$  for each ionization category. If the r.m.s. error for an individual line is  $\pm 8.6$  mas as suggested above, then the formal averages are  $203 \pm 2.5$  mas for ionization category A ( $N = 11$  spectral features) and  $229 \pm 3.5$  mas for

---

<sup>6</sup> Real positional differences may exist among the Fe II and [Fe II], but theoretically there should be almost no difference between lines 10 and 13 (multiplet 4F) or between lines 14 and 15 (multiplet 20F).



categories B and C together ( $N = 6$ ); a  $6\sigma$  difference. If, pessimistically but somewhat illogically, we base the individual measurement uncertainty on the larger scatter within data set  $B \cup C$ , then the difference is still  $3.4\sigma$ . If we omit the weakest lines in each category, or if we omit the intermediate category B, then the confidence level becomes stronger. In summary, the conclusion that  $\hat{z}(B \cup C) > \hat{z}(A)$  is quite well established so far as random errors are concerned.

The relatively large scatter in  $\hat{z}$  within categories B and C is not surprising. [Fe III] represents a lower-ionization zone than [Ne III], [Ar III], and He I, while all these lines span a range of temperature dependences.

#### 4.2. A different approach to statistical significance

If one is skeptical about the r.m.s. measurement errors reported above, another form of reasoning does not require them. Consider, for example, the following statement about the strongest emission lines, the filled symbols in Fig. 6. *All three of the  $\hat{z}$  values in ionization categories B and C exceed all five of those in category A.* If they were all random samples of one population, the probability of this outcome would be less than 0.02. This type of test is valid for any reasonable population distribution. The fainter lines strengthen the case. Suppose that the eleven measurements in category A and the six in categories B and C constitute two sets of random samples. (Differences in quality may alter this assumption, but more elaborate analyses lead to the same conclusion.) *All of the  $\hat{z}$  values in set  $B \cup C$  are higher than the second-largest value in set A.* If both sets were drawn from one population, the probability of this outcome would be less than 0.0006. If we further note that only one value in set  $B \cup C$  lies below the highest in set A, this becomes a problem in multinomial coefficients (e.g., DeGroot & Schervish 2002) and the probability falls below 0.0002. Set  $B \cup C$  thus differs from set A with a high confidence level, whether we use all

the spectral features or only the best ones. This statement does not require any knowledge of the measurement errors.

### 4.3. Concerning systematic errors

Although the measurement procedure was blind to ionization state as noted above, there is an obvious danger in the small number of suitable high-ionization features. Subtle effects involving location on the CCD detector might conceivably influence the results merely because the distribution of [Ne III], [Ar III], and [Fe III] lines was sparse. Fortunately we can assess this possibility via the low-ionization lines. In the best grating-tilt wavelength interval, 4565–4845 Å (Table 2), three category A lines have smaller wavelengths than [Fe III] and three have larger wavelengths; together they show no trend large enough to affect the result for [Fe III]. The 3795–4075 Å interval is less satisfactory because all three measureable category A lines there have longer wavelengths than [Ne III]  $\lambda$ 3870 – but the  $\hat{z}$  value for that feature is so large that a hypothetical wavelength-dependent effect would need to be far greater than any comparison lines suggest. A similar remark applies to [Ar III]. In summary: The low-ionization features appear to confirm what one expects from the nature of the instrument, i.e., that there is no serious wavelength-dependent error in our measurement procedure within each spectrogram.<sup>7</sup>

---

<sup>7</sup> Optical distortions are negligible in the narrow range of CCD rows used here, see the instrument handbook at [www.stsci.edu/hst/stis/handbooks/](http://www.stsci.edu/hst/stis/handbooks/). In order to nullify the [Ne III] result, one would need a spatial-scale variation of the order of 10% between 3870 Å and 4000 Å.

#### 4.4. Other potentially important findings

Weigelt knot C is partially resolved in the light of emission lines, with FWHM  $\sim 180$  mas compared to about 80 mas for the star image. Therefore the true, deconvolved FWHM is probably between 150 and 170 mas, or about 370 AU at  $\eta$  Car’s distance. Near-IR data give the same extent for dust in the knot, see Figure 4 in Artigau et al. (2011). Ionization categories A, B, C, and D spatially overlap each other to a great extent. This is not surprising, since we view the ionization structure from an oblique angle relative to the star-knot radial vector. Note, however, that the spatial profiles for [Ne III] and [Ar III] are strongly skewed toward larger  $z$ . This fact by itself is enough to distinguish those two highest-ionization features from most of the others. On average the low-excitation emission appears skewed in the opposite direction. We have not attempted to model the asymmetric spatial profiles shown in Figures 4 and 5.

Those figures also show a second obvious brightness peak around  $z \approx 8.4$  pixels  $\approx 430$  mas. Based on this and previous hints (e.g., §3.2 in Mehner et al. 2010), evidently the emission morphology has numerous local spots, not just the three classic Weigelt knots. The example shown in our data must be roughly aligned with the star and Knot C. Faint material can be perceived near that location in some *HST* images (Smith et al. 2004), but it seems uncertain there for the reasons noted in (§2) above. In any case the STIS results define this outer knot fairly well, and they show that it is almost half as bright as Knot C in emission-line categories B, C, and D (Figs. 4 and 5). Since the outer knot does not show a clear peak in the lower ionization features, we did not attempt to detect ionization structure there. The most effective way to map the region is to use STIS spectra with spatial dithering parallel to the slit – another task that no one has attempted.

Small Doppler velocity effects may accompany the positional differences shown in Fig. 6. Measurements using ordinary methods show no significant velocity trends among the

categories of emission lines, but the differences may be too small to detect routinely. The individual lines’ velocity profiles probably differ as well. A special velocity investigation with unusually precise wavelength calibrations, etc., is beyond the scope of this paper, because it would require as much additional effort as the steps reported above. Zethson (2001) and Zethson et al. (2012) list many emission velocities in the Weigelt knots with ordinary accuracy, including all the features in Table 1.

## 5. Discussion

The unexpectedly inverted excitation structure – with higher-ionization species relatively farther from the star rather than closer – is not easy to explain. Very likely it is a clue to some previously unrecognized aspect of the Weigelt knots’ morphology.

The most obvious idea, excitation by an outer bow shock, fails for at least two reasons. First, this conjecture would require ambient gas moving either *slower* than Knot C relative to the star, or else inward. Since the knots’ velocities are themselves very slow in the context of  $\eta$  Car, and the vicinity should have been swept out by two eruptions and the stellar wind, this seems very unlikely. There is no emission-line evidence for motionless or inward-moving gas. A second objection concerns the energy budget. The mass of visible, unobscured material in Weigelt knots B, C, and D is of the order of  $0.01 M_{\odot}$  (Hamann 2012; Davidson et al. 1995), implying kinetic energy  $\sim 10^{44}$  ergs at the observed speed of roughly  $40 \text{ km s}^{-1}$ . Even if this is converted into emission lines within only 100 years, the total luminosity of all the lines would be less than  $10^{34.6}$  ergs  $\text{s}^{-1}$ , several orders of magnitude too small. Moreover, this is an optimistic estimate since the knots do not appear to be decelerating that rapidly, and because most of the energy of a shock dissipates through expansion rather than line emission. The bow-shock idea therefore appears highly implausible.

Lesser shocks or other material waves moving through the knots are similarly unappealing. In order to excite even a fraction of the observed emission, they would need to carry so much energy and momentum that the knots would be disrupted within a few years. UV photons from the star, on the other hand, can heat and excite the knots because they carry far less momentum per unit energy.

Most likely, some relatively low-density high-ionization zones exist around knot C, with a geometry that somehow allows most of the photoionizing energy to be reprocessed in regions slightly farther from the star than is the center of the knot. It would be useful to have spatial measurements along a slit perpendicular to the orientation that we used, but unfortunately no such data exist.

Figure 7 shows one specific possibility. When a gas condensation is illuminated by ionizing photons, heated material can “evaporate” through an expansion front. In favorable circumstances the escaping gas flows outward around the condensation, accelerated by radiative forces exerted via photoionization: zone 2 in the figure. One might call this process photo-ablation or photo-evaporation, and it can produce a rocket effect that we are not concerned with here. Because zone 2 is less dense and is directly exposed to the central star, it should produce mainly high-ionization category-C emission lines. As Figure 7 illustrates, emission lines from zone 2 may appear preferentially on the *outer* side of the condensation itself (zone 1), in our projected view.

Admittedly the densest emission region should be near the expansion front, adjoining the inner edge of zone 1. The basic idea nevertheless remains viable, because those inward-facing regions may be partially obscured by dust in the condensation, and also for reasons involving the density-dependent [Ne III] and [Ar III] emissivities. A detailed model of the accelerated flow is needed in order to say whether the high-ionization lines should exhibit conspicuous velocity differences. If an explanation of this type is true, then it is

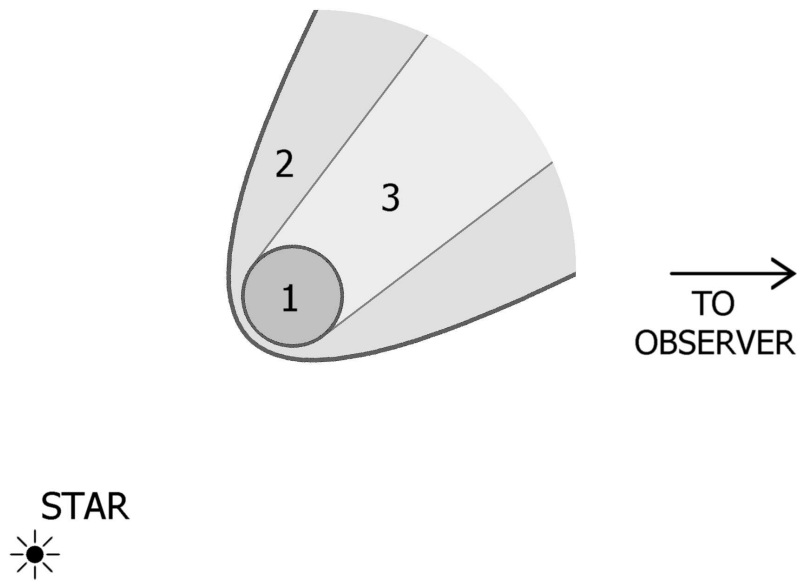


Fig. 7.— “Ablation” caused by photoionization. Zone 1 is a dense low-ionization cloud, zone 2 contains outward-flowing gas photoionized by the star, and zone 3 is shadowed. Emission lines from zone 2 might on average originate higher than zone 1 in this diagram, see text. This is merely a qualitative sketch of one possibility.

potentially useful because the partially observable structure depends on parameters of the knot.

Conceivably a separate, unrelated *high-ionization* knot lies along a line of sight slightly farther from the star than the center of knot C, thereby perturbing our [Ne III] and [Ar III] measurements. But this idea is somewhat artificial, because the hypothetical condensation must have a particular column density and scale size in order to produce enough localized high-ionization emission without comparable low-ionization features. A large, low-density cloud, for instance, could produce [Ne III] but its spatial gradients would be insufficient for the proposed effect. High-ionization knots have not been obvious in the large volume of existing STIS data near  $\eta$  Car. If the true explanation is in this vein, then it strongly suggests a widespread, highly inhomogeneous configuration of low-speed ejecta. One good test would be to examine Weigelt knot D, see a later comment below.

In an unconventional view, the Weigelt brightness peaks may represent minima in the intervening extinction, not physical condensations. We do not advocate this idea here, and we have not attempted to construct such a model, but it has not been ruled out and it would fundamentally alter the meanings of Figure 6 and Table 4. This question needs more comparisons between *HST* and IR maps (cf. Artigau et al. 2011). Precise Doppler velocities are worth investigating as noted in §4.4.

The spatial profiles in Figures 4 and 5 have other interesting implications. For example the Weigelt knots originally appeared to be small condensations (Weigelt & Ebersberger 1986; Hofmann & Weigelt 1988), but in fact they have widths almost half as large as their distances from the star (§4.4 above, and Fig. 4 in Artigau et al. 2011). This fact obviously affects theories of their origin and makes their proper motions more difficult to quantify (§2 above).

In Table 4, entries I1 and I2 are two estimates of  $\hat{z}$  for dust in Knot C, based on

published measurements of non-spectroscopic images. Various emission lines also contribute, but the images were most likely dominated by hot-dust emission for I1 and dust reflection for I2. Chesneau et al. (2005) and Artigau et al. (2011), discussing the near-IR data used for position I1, carefully referred to knot  $C'$ , not  $C$ , to distinguish between the locations of dust emission and reflection. Thus it makes sense that  $\hat{z}$  for knot  $C'$  (I1 in Table 4) is larger than the value for low-excitation emission lines. The I2 value, on the other hand, appears surprisingly large at 237 mas. It was based on *HST* images (Smith et al. 2004), and in a simple model it should have been in the neighborhood of 220 mas. We cannot explore this question here, but a likely guess is that irregularities in the p.s.f. and other subtleties in the central star image led to systematic errors as hinted in §2 above. This issue matters because the often-quoted Smith et al. (2004) analysis of the knots' proper motions and age relied on the same images and measurement techniques.

The other well-defined Weigelt knot, knot D, should be examined for ionization structure in the same way as knot C. Unfortunately we have not been able to obtain *HST* observing time for suitably dithered observations. As a conceivable alternative approach, one might employ a large set of existing data. Many STIS observations of  $\eta$  Car in 1998–2011 used a slit position angle near  $331^\circ$  which samples knot D, see Mehner et al. (2010) and refs. therein. At a subpixel level, those data have more or less random placements of the star and knot along the slit – a form of accidental spatial dithering. However, since the star/knot brightness ratio has varied and we have no assurance that the knot's spatial profile has remained constant, a careful investigation along these lines would require more effort than the knot C analysis presented above.

In approximately the same manner as our ionization-zone analysis, *HST*/*STIS* data may be useful for two obvious additional tasks. First, this appears to be the best way to measure the Weigelt knots' proper motions and age at UV to red wavelengths. The main



obstacle is a limited temporal baseline, beginning no earlier than 1998. Existing data near slit position angle  $331^\circ$  (see above) are pertinent in this connection. In principle, “virtual dithering” for each observation date might be obtained by using separate emission lines which peak at different fractional-row locations because of the slope of the spectral trace (§3.1).

A second interesting goal would be to map the region within  $1''$  of  $\eta$  Car in somewhat the same way as Mehner et al. (2010) but with higher spatial resolution. The fainter knot beyond C (Figures 4 and 5) is one example of why this would be useful; multiple brightness peaks in the region are very poorly known. This goal requires STIS observations that are spatially dithered along the slit, arguably more essential than dithering perpendicular to it. Unfortunately no such data exist at present, except those used in this paper.

#### *Acknowledgements*

GNR is supported by a Hertz Foundation Fellowship. We thank Beth Perriello and other consultants at STScI for assistance with the *HST* observing techniques.

## REFERENCES

- Artigau, É., Martin, J.C., Humphreys, R.M., Davidson, K., Chesneau, O., & Smith, N. 2011, *AJ*, 141, art. 202
- Chesneau, O., et al. 2005, *A&A*, 435, 1043
- Davidson, K., Ebbets, D., Weigelt, G., et al. 1995, *AJ*, 109, 1784
- Davidson, K., Ebbets, D., Johansson, S., Morse, J.A., & Hamann, F.W. 1997, *AJ*, 113, 335
- Davidson, K. 2006, in *The 2005 HST Calibration Workshop*, ed. A.M. Koekemoer, P. Goudfrooij, & L.L. Dressel (Baltimore, MD: STScI), 247
- Davidson, K., & Netzer, H. 1979, *Revs. Mod. Phys.* 51, 715
- Dorland, B.N., Currie, D.G., & Hajian, A.R. 2004, *AJ*, 127, 1052
- DeGroot, M.H., & Schervish, M.J. 2002, *Probability and Statistics, Third Edition*, §1.9 (Boston:Addison-Wesley), 35
- Hamann, F. 2012, in *Astroph. & Space Sci. Library 384, Eta Carinae and the Supernova Impostors*, ed. K. Davidson & R.M. Humphreys (New York: Springer), 95
- Hofmann, K.-H., & Weigelt, G. 1988, *A&A*, 203, L21
- Johansson, S., & Hamann, F.W. 1993, *Physica Scripta*, T47, 157
- Johansson, S., & Letokhov, V.S. 2004, *A&A*, 428, 497
- Krist, J.E., Hook, R.N., & Stoehr, F. 2011, *Proc. SPIE 8127*, 81270J
- Mehner, A., Davidson, K., Ferland, G.J., & Humphreys, R.M. 2010, *ApJ*, 710, 729

- Osterbrock, D.E., & Ferland, G.J. 2006, *Astrophysics of Gaseous Nebulae and Active Galactic Nuclei* (Sausalito, CA: University Science Books)
- Smith, N., Morse, J.A., Gull, T.R. 2004, *ApJ*, 605, 405
- Smith, N. 2012, in *Astroph. & Space Sci. Library 384, Eta Carinae and the Supernova Impostors*, ed. K. Davidson & R.M. Humphreys (New York: Springer), 145
- Verner, E., Bruhweiler, F., & Gull, T. 2005, *ApJ*, 624, 973
- Weigelt, G., & Ebersberger, J. 1986, *A&A*, 163, L5.
- Weigelt, G., Albrecht, R., Barbieri, C., et al. 1995, *RevMexAA Conf. Ser.* 2, 11
- Weigelt, G., & Kraus, S. 2012, in *Astroph. & Space Sci. Library 384, Eta Carinae and the Supernova Impostors*, ed. K. Davidson & R.M. Humphreys (New York: Springer), 129
- Zethson, T. 2001, PhD thesis, Lunds Univ., Sweden
- Zethson, T., Johansson, S., Hartman, H., & Gull, T.R. 2012, *A&A*, 540, A133

Table 1. Narrow Emission Lines Measured in Weigelt Knot C

Label & category <sup>a</sup>	ID <sup>b</sup>	$\lambda_{\text{vac}}$ (Å)	Transition <sup>b</sup>	$E_2^c$ (eV)	$E_1^c$ (eV)
1 D	Fe II	2507.55	$c^4F_{7/2} - 5p^6F_{9/2}$	11.167	6.222
2 D	Fe II	2509.10	$c^4F_{7/2} - 4p^4G_{9/2}$	11.164	6.222
3 C	[Ne III] (1F)	3869.85	$2p^4\ ^3P_2 - 2p^4\ ^1D_2$	3.204	0
4 A	Fe II (3)	3939.41	$a^4P_{5/2} - z^6D_{5/2}$	4.818	1.671
5 A	[Ni II] (3F)	3994.19	$a^2D_{5/2} - b^2D_{5/2}$	3.104	0
6 C	He I (18)	4027.33	$2p\ ^3P - 5d\ ^3D$	24.043	20.964
7 A	[S II] (1F)	4069.75	$3p^3\ ^4S_{3/2} - 3p^3\ ^2P_{3/2}$	3.046	0
8 A	Fe II (38)	4585.12	$b^4F_{9/2} - z^4D_{7/2}$	5.511	2.807
9 A	Fe II (37)	4630.64	$b^4F_{9/2} - z^4F_{9/2}$	5.484	2.807
10 A	[Fe II] (4F)	4640.97	$a^6D_{3/2} - b^4P_{1/2}$	2.778	0.107
11 B	[Fe III] (3F)	4659.35	$3d^6\ ^5D_4 - 3d^6\ ^3F_4$	2.661	0
12 B	[Fe III] (3F)	4702.85	$3d^6\ ^5D_3 - 3d^6\ ^3F_3$	2.690	0.054
13 A	[Fe II] (4F)	4729.39	$a^6D_{5/2} - b^4P_{3/2}$	2.704	0.083
14 A	[Fe II] (20F)	4776.05	$a^4F_{9/2} - b^4F_{7/2}$	2.828	0.232
15 A	[Fe II] (20F)	4815.88	$a^4F_{9/2} - b^4F_{9/2}$	2.807	0.232
16 C	He I (10)	7067.20	$2p\ ^3P - 3s\ ^3S$	22.718	20.964
17 C	[Ar III] (1F)	7137.76	$3p^4\ ^3P_2 - 3p^4\ ^1D_2$	1.737	0
18 A	[Fe II] (14F)	7157.13	$a^4F_{9/2} - a^2G_{9/2}$	1.964	0.232
19 A	[Fe II] (14F)	7173.98	$a^4F_{7/2} - a^2G_{7/2}$	2.030	0.301

<sup>a</sup>A,B,C = low, moderate, or high ionization, D = “exotic,” see text.

<sup>b</sup>Zethson (2001); Zethson et al. (2012).

<sup>c</sup>[http://physics.nist.gov/PhysRefData/ASD/levels\\_form.html](http://physics.nist.gov/PhysRefData/ASD/levels_form.html).

Table 2. Dithered HST/STIS/CCD Observations<sup>a</sup>

Root number <sup>b</sup>	Wavelength Range (Å)	Position <sup>c</sup> (pixels)	$\Delta t^d$ (s)	$N^e$
ob6064150	2480–2680	510.129	200	2
ob6064160	"	514.641	200	2
ob60640s0	3795–4075	514.995	6	2
ob60640u0	"	519.488	6	2
ob60640t0	"	515.031	54	3
ob60640v0	"	519.534	54	3
ob60640j0	4565–4845	513.161	10	2
ob60640l0	"	517.648	10	2
ob60640k0	"	513.183	60	4
ob60640m0	"	517.681	60	4
ob60641b0	7000–7565	517.615	21	3
ob60641d0	"	522.122	21	3

<sup>a</sup>Obs. 2010 March 3, MJD 55258.7 = J2010.17, HST Program GO 11612 (PI = K. Davidson).

<sup>b</sup>ID label in the HST archive.

<sup>c</sup>“Position” means the measured CCD row number of the central star continuum ( $x_A$  in Fig. 1 and §3.1) at column 494 near the middle of the CCD. The nominal row width was 50.71 mas, the slit width was 100 mas, its position angle was  $301.95^\circ$ , and an initial peakup was used to place the central star as close to the slit midline as possible.

<sup>d</sup>Integration time (= total exposure time).

<sup>e</sup> $N$  = CR-SPLIT, the number of separate exposures combined to make an “observation.”

Table 3. Measured Positions

	Feature and category <sup>a</sup>		$u^b$	Peak <sup>c</sup>	$z_c^d$	$z_m^d$	err <sup>e</sup>
1	Fe II $\lambda$ 2508	D	183	4350	4.426	4.394	$\pm.06$ :
2	Fe II $\lambda$ 2509	D	193	5660	4.256	4.290	$\pm.06$ :
3	[Ne III] $\lambda$ 3870	C	269	3320	4.844	4.740	$\pm.055$
4	Fe II $\lambda$ 3939	A	519	890	3.939	3.990	$\pm.100$
5	[Ni II] $\lambda$ 3994	A	717	670	4.270	4.269	$\pm.120$
6	He I $\lambda$ 4027	C	836	730	4.258	4.332	$\pm.120$
7	[S II] $\lambda$ 4070	A	990	1310	4.138	4.216	$\pm.085$
8	Fe II $\lambda$ 4585	A	91	2570	3.869	3.946	$\pm.060$
9	Fe II $\lambda$ 4631	A	255	1830	3.698	3.671	$\pm.070$
10	[Fe II] $\lambda$ 4641	A	293	890	4.073	4.130	$\pm.100$
11	[Fe III] $\lambda$ 4659	B	359	1880	4.182	4.310	$\pm.070$
12	[Fe III] $\lambda$ 4703	B	516	770	4.384	4.325	$\pm.110$
13	[Fe II] $\lambda$ 4729	A	612	1860	3.895	3.997	$\pm.070$
14	[Fe II] $\lambda$ 4776	A	781	850	3.766	3.721	$\pm.110$
15	[Fe II] $\lambda$ 4816	A	926	2640	3.990	4.026	$\pm.060$
16	He I $\lambda$ 7067	C	127	2430	4.396	4.332	$\pm.060$
17	[Ar III] $\lambda$ 7138	C	254	780	5.102	5.023	$\pm.110$
18	[Fe II] $\lambda$ 7157	A	289	3330	4.152	4.161	$\pm.055$
19	[Fe II] $\lambda$ 7174	A	319	970	4.084	4.091	$\pm.100$

<sup>a</sup>See Table 1.

<sup>b</sup>Approximate STIS/CCD column (1–1024), cf. Table 2.

<sup>c</sup>Approximate maximum net counts per data point in Knot C.

<sup>d</sup>Centroid and midpoint distances from the star, expressed in CCD pixels ( $\sim 50.7$  mas).

<sup>e</sup>Estimated r.m.s. statistical errors in  $z$ , not including systematic effects which may be larger.

Table 4. Measured Distances from the Star

Ionization category <sup>a</sup>	$n_{\text{lines}}$ <sup>a</sup>	Median $\hat{z}$ (mas) <sup>b</sup>	Range of values (mas)
A	11	204	187 – 217
B	2	218	216 – 221
C	4	232	218 – 257
C <sup>c</sup>	2	249	243 – 257
D	2	220	216 – 224
I1 <sup>d</sup>	(dust?)	(229)	—
I2 <sup>e</sup>	(dust?)	(237)	—

<sup>a</sup>See Table 1.

<sup>b</sup>Projected distance from star, assuming CCD pixel-width = 50.71 mas.

<sup>c</sup>Omitting He I for reasons noted in §4.

<sup>d</sup>I1 = location of knot C' in Chesneau's 2002–2005 near-IR image data, corrected for expansion to 2010. See Fig. 4 in Artigau et al. (2011).

<sup>e</sup>I2 = location in 2010 “predicted” from HST image data, probably less accurate than I1. See Fig. 11 in Smith et al. (2004).